Realization of a 2D Lieb lattice in a metal-inorganic framework with partial flat bands and topological edge states

Realization of a Two-Dimensional Lieb Lattice in a Metal-Inorganic Framework with Partial Flat Bands and Topological Edge States

Wenjun Wu,[#] Shuo Sun,[#] Chi Sin Tang,[#] Jing Wu, Yu Ma, Lingfeng Zhang,* Chuanbing Cai, Jianxin Zhong, Milorad V. Milošević, Andrew T. S. Wee, Xinmao Yin**

W. Wu, S. Sun, Y. Ma, L. Zhang, C. Cai, X. Yin

Department of Physics, Shanghai Key Laboratory of High Temperature Superconductors, Shanghai University, Shanghai 200444, China
E-mail: physunshuo@shu.edu.cn; lingfeng_zhang@shu.edu.cn; yinxinmao@shu.edu.cn

C. S. Tang

Singapore Synchrotron Light Source (SSLS), National University of Singapore, Singapore 117603, Singapore

J. Wu

Institute of Materials Research and Engineering (IMRE), Agency for Science, Technology and Research (A*STAR), 2 Fusionopolis Way, Innovis #08-03, Singapore 138634, Singapore

J. Zhong

Center for Quantum Science and Technology, Department of Physics, Shanghai University, Shanghai 200444, China

M. V. Milošević

Department of Physics & NANOlab Center of Excellence, University of Antwerp, Groenenborgerlaan 171, B-2020 Antwerp, Belgium

A. T. S. Wee

Department of Physics, Faculty of Science, National University of Singapore, Singapore 117542, Singapore

A. T. S. Wee

Centre for Advanced 2D Materials and Graphene Research, National University of Singapore, Singapore 117546, Singapore

Abstract: Flat bands and Dirac cones in materials are at the source of the exotic electronic and topological properties. The Lieb lattice is expected to host these electronic structures, arising from quantum destructive interference. Nevertheless, the experimental realization of a two-dimensional Lieb lattice remained challenging to date due to its intrinsic structural instability. After computationally designing a Platinum-Phosphorus (Pt-P) Lieb lattice, we have successfully overcome its structural instability and synthesized it on a gold substrate via molecular beam epitaxy. Low-temperature scanning tunneling microscopy and spectroscopy verify the Lieb lattice's morphology and electronic flat bands. Furthermore, topological Dirac edge states stemming from pronounced spin-orbit coupling induced by heavy Pt atoms have been predicted. These findings convincingly open perspectives for creating metal-inorganic framework-based atomic lattices, offering prospects for strongly correlated phases interplayed with topology.

Keywords: flat bands, Lieb lattice, scanning tunneling microscopy, Dirac edge states, metal-inorganic framework

1. Introduction

Electronic flat bands (FBs) in momentum space, when combined with strong electron-electron interactions, are known to foster unconventional superconductivity,[1,2] fractional quantum Hall effect,[3,4] room-temperature ferromagnetism,[5,6] the formation of Wigner crystals,[7,8] excitonic insulator state[9] and excitonic Bose-Einstein condensation.[10] It has been demonstrated that the strongly correlated states observed in moiré systems such as correlated insulating states and unconventional superconductivity are related to FBs. For example, the magic-angle twisted bilayer graphene displays correlated insulating states at half-filling of FBs, and transitions into a superconducting state when charge carriers are introduced.[1,2] Nevertheless, up to date, the experimental realization of FBs is still limited to moiré systems and artificial systems. It should be noted that the relatively large unit cell of the moiré systems leads to a low electron density, which may hinder the emergence of the physics typically observed in high-electron-density systems. Hence, it is of significance to construct FBs in the non-moiré solid materials.

Theoretically, FBs naturally emerge in geometrically frustrated lattices due to quantum destructive interference.[11,12] One of the notable examples of such frustrated geometries is the Lieb lattice,[13] a two-dimensional (2D) edge-centered square lattice, which is also known for its association with the CuO_2 planes of cuprate high-temperature superconductors.[14] With each unit cell containing one corner site and two edge-centered sites (**Figure 1**, a and b), the Lieb

lattice exhibits unique electronic properties including FBs, Dirac cones and saddle-point van Hove singularities (VHSs) (Figure 1, a and c), wherein, the nearest-neighbor electron hoppings are taken into account in tight-binding methodology.[12] Additionally, the presence of Dirac cones is associated with high carrier mobility and nontrivial topological properties,[15,16] offering promising prospects for a wide range of applications in electronic devices,[17] topological catalysis,[18] batteries,[19] and supercapacitors.[20] Up to date, the Lieb lattice has primarily been designed in artificial systems due to its intrinsic structural instability, including molecular patterning on metal substrates,[21-23] photonic waveguide arrays,[24,25] cold atom systems,[26] covalent-organic frameworks (COFs)[27-29] and metal-organic frameworks (MOFs).[30] Nevertheless, sustained difficulties in the experimental realization of the Lieb lattice in real solid materials have limited an in-depth exploration of its exotic quantum states that may carry strong implications for both fundamental scientific research and practical applications. Notably, the physical and chemical properties of Lieb-like lattices constructed by COFs or MOFs are easily tunable via strain engineering techniques, doping, and by changing different organic ligands, but the relatively large hopping distances and the complexity of multiple hopping parameters considered in COFs and MOFs have greatly hampered the study of their electronic properties.[27,28,30] Meanwhile, the physical and chemical properties of Lieb lattices based on metal-inorganic frameworks (MIFs) remained widely elusive. Recently, the successful realization of buckled Lieb lattices (Sn-Al) using molecular beam epitaxy (MBE), which relies on the interaction between specific atoms and a metal surface, has sparked significant interest.[31] However, the characteristic electronic properties of the Lieb lattice including FBs, Dirac cones and VHSs, have not been found in the Sn-Al lattice. Continued efforts are thus needed to synthesize the high chemical stability of novel Lieb lattices and uncover their advanced electronic and topological properties.

Under specific conditions, a Lieb lattice can be epitaxially formed, as illustrated in Figure 1a, facilitated by strong interactions between purple and blue atoms, driven by their distinct electronegativity.[32] The purple atoms are chosen for their high chemical stability to occupy the hollow sites of the blue atoms. Meanwhile, the golden atoms act as a supportive substrate and provide the foundation for epitaxial growth. In this case, platinum has been selected as the purple atoms due to its exceptional stability, while phosphorus is chosen as the blue atoms for its strong affinity with metals, which facilitates the formation of coordination bonds. Gold serves as the substrate layer for its stability and conductivity, thereby bearing in mind the prospect of using Lieb lattices in electronic devices and applications.

With above choices made, we report here the successful *ab initio* computational design of the Platinum-Phosphorus (Pt-P) Lieb lattice based on a MIF, which possesses quintessential properties including partial FBs, Dirac cones, and VHSs in its electronic band structure. Such Pt-P Lieb lattice was then prepared on an Au(111) substrate via MBE. Subsequent thorough experimental characterization including atomically-resolved scanning tunneling microscopy (STM) imaging and high-resolution scanning tunneling spectroscopy (STS) fully corroborates the structural morphology and the presence of electronic FBs of the Pt-P Lieb lattice, as predicted by theoretical calculations. We further argue the existence of a topological Dirac edge state in this Pt-P Lieb lattice due to the strong spin-orbit coupling (SOC) effect imparted by the heavy Pt atoms. These results unequivocally prove the potential that MIF-based Lieb lattices hold for delving into FB physics and the exploration of nontrivial topological phenomena, up to the standards of technological needs.

2. Results

2.1. Crystal structures and electronic properties of the Lieb lattice

Figure 2, a and b, displays the atomic model of Pt and P adlayers on an Au(111) substrate. P (cyan) and Pt (orange) atoms form the 1×1 and $\sqrt{2} \times \sqrt{2}$ square-like lattice, respectively, such that the Pt atoms are located at the four-hollow sites of P atoms. As shown in Figure 2c, with increasing interlayer distance, the interlayer binding energy (E_b) exhibits a parabolic-like decrease, followed by a linear increase. Our theoretical simulations reveal that the energetically ideal interlayer distances are $d_1 = 0.8$ Å and $d_2 = 2.2$ Å, for which the Pt (P) atoms are arranged in a square-like lattice with the nearest Pt-Pt (P-P) distance of 3.8 Å (2.2 Å). The phonon dispersion curves of the Pt-P Lieb lattice are calculated based on density functional perturbation theory,[33] showing that imaginary phonon modes appear at the Y and M points (see Figure S6). Notably, it reveals a trend towards effective mitigation on the Au substrate. Therefore, Pt and P adlayers form a 2D Lieb lattice, different from the Sn-Al lattice relying on the Sn adlayer and the topmost Al atoms as realized in Ref. 31.

To investigate electronic properties of the 2D Pt-P Lieb lattice, we compare the band structures without and with SOC effects included, as depicted in Figure 2, d and e, respectively. Although the strong SOC effect from heavy Pt atoms leads to prominent changes to several energy bands, distinctive band features in the form of partial FBs, VHSs and Dirac points that characterize the Pt-P Lieb lattice remain present. Specifically, seven nearly dispersionless FBs are distributed above and below the Fermi level (E_F). These partial FBs (dashed purple squares

in Figure 2, d and e) give rise to distinctive peaks in the computed projected density of states (see Figure S1), and consist primarily of contributions from the P 3*p* orbitals and Pt 5*d* orbitals. However, we find *p*-*d* orbital overlaps in the orbital-decomposed band structure, as depicted in Figure S1. For example, the P p_y-Pt d_{xy} orbital overlaps appear at ~E_F +2.12 eV. Consequently, the orbital symmetry interferes with the lattice symmetry, leading to the formation of FBs that are restricted to a segment of the whole Brillouin zone, representing partial FBs. Notably, lattice intercalation serves as an effective strategy for mitigating this situation, offering the potential to the isolation of ideal FBs[34] or the realization of yin-yang FBs.[35] Meanwhile, the VHS (dashed red circle) is manifested in much flatter dispersion along X-M as compared to the direction X-Γ (see Figure S2). This suggests that the quadratic contribution along X-M is substantially reduced. Intriguingly, the VHSs located near E_F can serve as a potential carrier reservoir, thereby enhancing the superconductivity and catalytic properties of the host material.[36,37] Additionally, strongly dispersive Dirac cones (dashed blue and green circles) located at the Y-point near E_F, may present nontrivial topological properties when the SOC effect is present as further discussed thereafter.

2.2. Experimental realization of Lieb lattices in a MIF

With the encouraging results from theoretical calculations, epitaxial growth of P and Pt adlayers on an Au(111) substrate has been systematically carried out. After the deposition of 1 monolayer of P onto a clean Au(111) surface and subsequent annealing at 300 °C, Pt atoms were deposited, and annealed at 300 °C for 80 minutes (**Figure 3**a). From the magnified high-resolution STM image in Figure 3b, one can clearly see the bright region formed. The measured distance between Pt adlayers and Au(111) surface is ~3.0 Å, corresponding to the theoretical calculations (see Figure 2c and Figure S3). Figure 3, c and e, represents an atomically resolved STM image of one such region, revealing that the short-range ordered Lieb lattice with convincingly square-shaped geometry is formed there, where the bright dots represent the Pt atoms. Notably, the epitaxial growth of P and Pt atoms on the Au (111) substrate follows the same trend as the deposition of P atoms on the Pt (111) substrate,[38] with Pt atoms exhibiting the square lattice morphology. In this case, the Pt-P Lieb lattice exhibits slight deformation owing to its intrinsic structural instability and lattice mismatch. Some point defects are visible as well (dark pits in Figure 3c), which in fact may optimize the charge carrier concentration and scattering of high-frequency phonons, and thus improve some materials' properties.[39] The close-up STM images in the dark region adjacent to the Lieb lattice reveal that Pt atoms were deposited on the Au(111) surface (see Figure S7). The Pt adlayer exhibits a hexagonal shape,

aligning with the close-packed atomic arrangement of the Au(111) substrate.[40,41] The differential conductance curve (dI/dV) measured by STS for the sites within the Lieb lattice of Figure 3c is displayed in Figure 3d. Two sharp peaks proportional to density of states (DOS) are observed, one at $V \approx +2.66$ V and one at $V \approx +1.83$ V, corresponding to partial FB1-2 (~E_F +2.98 eV) and partial FB3 (~E_F +2.12 eV) in the calculated band structure (see Figure S1), respectively. Additionally, Lieb lattices were also discerned in other regions via close-up STM imaging (see Figure S8 and S9), with the dI/dV spectrum revealing two peaks (see Figure S8). And the bright features at the periphery of the Lieb lattice, delineated by blue dashed lines, indicate the presence of edge states (see Figure S9). Nevertheless, the insensitivity of states near and below E_F in this system complicate experimental measurements, resulting in the non-observation of the expected FB peaks. Such cases can also appear in the kagome,[42-44] Lieb,[22] and coloring-triangle lattice.[45]

Further STM simulation was conducted based on an optimized geometric model with the simulated STM image based on the Tersoff-Hamann method within constant current mode shown in Figure 3g.[46] In this case, with the bright dots representing the Pt atoms, it is in good agreement with the experimental results (Figure 3, c and e) and crystal structures (Figure 3f). The distance between adjacent Pt atoms is measured to be ~4.0 Å (see Figure S3), close to the Pt-Pt bond length of ~3.8 Å within structural optimization. This further supports the reliability of our theoretical model.

2.3. Nontrivial topological properties of the Pt-P Lieb lattice

To further explore the nontrivial topological properties of the Pt-P Lieb lattice, we have conducted calculations to investigate its surface and edge states, in particular with the important role that SOC of the heavy elements plays in the band structures near E_F. Nontrivial topological effects such as band opening and band inversion are expected to take place,[47] further enabling exotic quantum phenomena.[48] This is particularly true in the present case, where the Pt atom as a heavy elemental component has associations with triply degenerate semimetals and multifold degenerate semimetals.[49,50] In our calculations, the two Dirac cones at the Y-point near E_F, as seen in Figure 2d, are particularly interesting. Hence, with the SOC effect considered, there are bandgap openings at the Dirac cone located at ~E_F -0.18 eV and ~E_F +0.26 eV by about ~38 and ~6 meV, respectively (see Figure S4). These are direct signatures of nontrivial topological properties. **Figure 4**, a and b, provides further details of the energy dispersion function along the (100) surface that corresponds to the Dirac cone below and above E_F,

respectively. In each case, the edge states are clearly visible as indicated by the red contours in Figure 4, c and d. Interestingly, Figure 4c exhibits a Dirac-cone edge state (in red) at E_F, thereby facilitating the flow of electrons from the valence band to the conduction band. Figure 4d shows two edge states (in red) that connect both the bottom and top bands. Even though the edge states are located above E_F, their locations can be tuned to the E_F position via strain engineering,[51] doping,[52] multilayer stacking,[53] and applying electric fields.[54] This further enhances its potential for applications in devices, catalysis and energy storage. To verify topologically nontrivial edge states of the Lieb lattice, we calculated the Z_2 topological invariants using the WannierTools package.[55] The Wilson loop method is employed to track the evolution of the Wannier charge centers,[56] which confirmed the nontrivial topological properties of the Lieb lattice with a nonzero $Z_2 = 1$ (see Figure S5).

3. Conclusion

In summary, we have successfully designed a 2D Pt-P Lieb lattice based on first-principles calculations, where unique electronic properties such as partial FBs, Dirac cones, and VHSs have been anticipated. Based on that in *silico* design, a 2D Pt-P Lieb lattice has been synthesized using MBE, its structure has been validated by STM, and electronic FBs have been detected by STS. Based on the theoretical calculations, we have further predicted the existence of a nontrivial topological Dirac edge state in this Pt-P Lieb lattice. These findings provide a broad platform for design, fabrication, and a comprehensive understanding of the physical and chemical properties of Lieb lattices and will stimulate further theoretical and experimental research on MIF-based Lieb lattices. In other words, our successful design and fabrication of a MIF-based Lieb lattice opens new frontiers in the exploration of special electronic, magnetic, optical and topological properties of high-quality and stable Lieb lattice structures, providing opportunities for their applications in advanced (opto)electronic devices, catalysis, and energy-related technologies.

4. Methods

4.1. Tight-binding calculations

We constructed a tight-binding model with D_{4h} symmetry, where two edge-centered sites (A/C) and one corner site (B) have a coordination number of two and four, respectively. The electronic properties of the Lieb lattice can be calculated from the following tight-binding Hamiltonian:

$$H = \sum_i \epsilon_i c_i^\dagger c_i - t \sum_{\langle i,j \rangle} (c_i^\dagger c_j + H.c.) - t' \sum_{\langle\langle i,j \rangle\rangle} (c_i^\dagger c_j + H.c.)$$

where ϵ_i is the on-site energy of site i; t and t' indicate nearest-neighbor $\langle i,j \rangle$ and next-nearest-neighbor $\langle\langle i,j \rangle\rangle$ hopping constants, respectively; $c_i^\dagger$ and c_i are the creation and annihilation operators of an electron on site i, respectively. The on-site energy difference between B and C sites is $\Delta E = \epsilon_B - \epsilon_C$. The Lieb lattice is studied with t' and ΔE equal to zero, and t is set with a negative value.

4.2. First-principles calculations

First-principles calculations based on density functional theory (DFT) were undertaken by using the Vienna ab initio simulation package (VASP),[57] adopting the projector-augmented wave method.[58] The exchange-correlation functional based on the generalized gradient approximation (GGA) in the form of the Perdew-Burke-Ernzerhof (PBE) functional,[59] was used for both structural optimizations and electronic structure calculations. The energy cutoff was set at 500 eV. The density of *k*-point grids in the Brillouin zone is 11 × 11 × 1. The convergence criteria for the structural relaxation were that the force and total energy were set to 0.001 eV/Å and 10^{-6} eV, respectively. The Wannier90 package was used to construct Wannier tight-binding models,[60] and the WannierTools package was used to calculate the surface spectral functions by using the iterative Green's function method.[55] The scanning tunneling microscopy simulation was performed by the Tersoff-Hamann method in a constant current mode.[46]

4.3. Sample preparation and characterization

The experiments were carried out using a UHV−STM conjoined molecular beam epitaxy system. A clean Au(111) surface was prepared by repeated Ar^+ bombardment (1.5 kV, 5×10^{-5} mbar) and subsequently annealed at 270 °C. P atoms were deposited on an Au(111) surface and subsequently annealed at 300 °C. Pt atoms were then deposited (10.0 Å 20 min + 10.2 Å 30 min) and annealed at 300 °C for 80 min. All the scanning tunneling microscopy and spectroscopy (STM/STS) measurements were carried out at 77 K with the bias voltage applied to the sample.

Data availability

All data supporting the findings of this study are available within the paper and its Supporting Information, or available from the corresponding authors upon reasonable request.

Acknowledgements

Wenjun Wu, Shuo Sun and Chi Sin Tang contributed equally to this work. This work was supported by National Natural Science Foundation of China(Grant Nos.52172271, 12374378, 52307026, 12374046),the National Key R&D Program of China (Grant No. 2022YFE03150200),Shanghai Science and Technology Innovation Program(Grant No. 22511100200, 23511101600). J.W. acknowledges the Advanced Manufacturing and Engineering Young Individual Research Grant (AME YIRG Grant No. A2084c0170) and the SERC Central Research Fund (CRF). C.S.T. acknowledges the support from the NUS Emerging Scientist Fellowship. S.S. acknowledges support from Natural Science Foundation of China (Grant No. 12304199), Science and Technology Commission of Shanghai Municipality, the Shanghai Venus Sailing Program (Grant No. 23YF1412600).

Conflict of Interest

The authors declare no competing interests.

References

[1] Y. Cao, V. Fatemi, S. Fang, K. Watanabe, T. Taniguchi, E. Kaxiras, P. Jarillo-Herrero, *Nature* **2018**, 556, 43.
[2] Y. Cao, V. Fatemi, A. Demir, S. Fang, S. L. Tomarken, J. Y. Luo, J. D. Sanchez-Yamagishi, K. Watanabe, T. Taniguchi, E. Kaxiras, R. C. Ashoori, P. Jarillo-Herrero, *Nature* **2018**, 556, 80.
[3] A. A. Zibrov, E. M. Spanton, H. Zhou, C. Kometter, T. Taniguchi, K. Watanabe, A. F. Young, *Nat. Phys.* **2018**, 14, 930.
[4] J. Léonard, S. Kim, J. Kwan, P. Segura, F. Grusdt, C. Repellin, N. Goldman, M. Greiner, *Nature* **2023**, 619, 495.
[5] C. Zhao, Z. Xu, H. Wang, J. Wei, W. Wang, X. Bai, E. Wang, *Adv. Funct. Mater.* **2014**, 24, 5985.
[6] G. Bouzerar, *Phys. Rev. B* **2023**, 107, 184441.
[7] H. Li, S. Li, E. C. Regan, D. Wang, W. Zhao, S. Kahn, K. Yumigeta, M. Blei, T. Taniguchi, K. Watanabe, S. Tongay, A. Zettl, M. F. Crommie, F. Wang, *Nature* **2021**, 597, 650.
[8] M. Shayegan, *Nat. Rev. Phys.* **2022**, 4, 212.
[9] G. Sethi, Y. Zhou, L. Zhu, L. Yang, F. Liu, *Phys. Rev. Lett.* **2021**, 126, 196403.
[10] G. Sethi, M. Cuma, F. Liu, *Phys. Rev. Lett.* **2023**, 130, 186401.
[11] N. Regnault, Y. Xu, M.-R. Li, D.-S. Ma, M. Jovanovic, A. Yazdani, S. S. P. Parkin, C. Felser, L. M. Schoop, N. P. Ong, R. J. Cava, L. Elcoro, Z.-D. Song, B. A. Bernevig, *Nature* **2022**, 603, 824.
[12] M. A. Springer, T.-J. Liu, A. Kuc, T. Heine, *Chem. Soc. Rev.* **2020**, 49, 2007.
[13] E. H. Lieb, *Phys. Rev. Lett.* **1989**, 62, 1201.
[14] A. Schilling, M. Cantoni, J. D. Guo, H. R. Ott, *Nature* **1993**, 363, 56.
[15] M. Z. Hasan, C. L. Kane, *Rev. Mod. Phys.* **2010**, 82, 3045.

[16] B. Q. Lv, T. Qian, H. Ding, *Rev. Mod. Phys.* **2021**, 93, 025002.
[17] O. Breunig, Y. Ando, *Nat. Rev. Phys.* **2022**, 4, 184.
[18] G. Li, C. Fu, W. Shi, L. Jiao, J. Wu, Q. Yang, R. Saha, M. E. Kamminga, A. K. Srivastava, E. Liu, A. N. Yazdani, N. Kumar, J. Zhang, G. R. Blake, X. Liu, M. Fahlman, S. Wirth, G. Auffermann, J. Gooth, S. Parkin, V. Madhavan, X. Feng, Y. Sun, C. Felser, *Angew. Chem. Int. Ed.* **2019**, 58, 13107.
[19] J. Liu, S. Wang, Q. Sun, *PNAS* **2017**, 114, 651.
[20] H. Luo, P. Yu, G. Li, K. Yan, *Nat. Rev. Phys.* **2022**, 4, 611.
[21] M. R. Slot, T. S. Gardenier, P. H. Jacobse, G. C. P. van Miert, S. N. Kempkes, S. J. M. Zevenhuizen, C. M. Smith, D. Vanmaekelbergh, I. Swart, *Nat. Phys.* **2017**, 13, 672.
[22] R. Drost, T. Ojanen, A. Harju, P. Liljeroth, *Nat. Phys.* **2017**, 13, 668.
[23] X. Li, Q. Li, T. Ji, R. Yan, W. Fan, B. Miao, L. Sun, G. Chen, W. Zhang, H. Ding, *Chin. Phys. Lett.* **2022**, 39, 057301.
[24] S. Mukherjee, A. Spracklen, D. Choudhury, N. Goldman, P. Öhberg, E. Andersson, R. R. Thomson, *Phys. Rev. Lett.* **2015**, 114, 245504.
[25] R. A. Vicencio, C. Cantillano, L. Morales-Inostroza, B. Real, C. Mejía-Cortés, S. Weimann, A. Szameit, M. I. Molina, *Phys. Rev. Lett.* **2015**, 114, 245503.
[26] S. Taie, T. Ichinose, H. Ozawa, Y. Takahashi, *Nat. Commun.* **2020**, 11, 257.
[27] W. Jiang, H. Huang, F. Liu, *Nat. Commun.* **2019**, 10, 2207.
[28] B. Cui, X. Zheng, J. Wang, D. Liu, S. Xie, B. Huang, *Nat. Commun.* **2020**, 11, 66.
[29] E. Jin, M. Asada, Q. Xu, S. Dalapati, M. A. Addicoat, M. A. Brady, H. Xu, T. Nakamura, T. Heine, Q. Chen, D. Jiang, *Science* **2017**, 357, 673.
[30] W. Jiang, S. Zhang, Z. Wang, F. Liu, T. Low, *Nano Lett.* **2020**, 20, 1959.
[31] H. Feng, C. Liu, S. Zhou, N. Gao, Q. Gao, J. Zhuang, X. Xu, Z. Hu, J. Wang, L. Chen, J. Zhao, S. X. Dou, Y. Du, *Nano Lett.* **2020**, 20, 2537.
[32] J. B. Mann, T. L. Meek, L. C. Allen, *J. Am. Chem. Soc.* **2000**, 122, 2780.
[33] S. Baroni, S. de Gironcoli, A. Dal Corso, P. Giannozzi, *Rev. Mod. Phys.* **2001**, 73, 515.
[34] D. Kim, F. Liu, *Phys. Rev. B* **2023**, 107, 205130.
[35] Y. Zhou, G. Sethi, C. Zhang, X. Ni, F. Liu, *Phys. Rev. B* **2020**, 102, 125115.
[36] Y. Luo, Y. Han, J. Liu, H. Chen, Z. Huang, L. Huai, H. Li, B. Wang, J. Shen, S. Ding, Z. Li, S. Peng, Z. Wei, Y. Miao, X. Sun, Z. Ou, Z. Xiang, M. Hashimoto, D. Lu, Y. Yao, H. Yang, X. Chen, H.-J. Gao, Z. Qiao, Z. Wang, J. He, *Nat. Commun.* **2023**, 14, 3819.
[37] L. Liu, C. Wang, L. Zhang, C. Liu, C. Niu, Z. Zeng, D. Ma, Y. Jia, *J. Phys. Chem. Lett* **2022**, 13, 740.
[38] J. Zhang, X. Dong, S. Xu, Y. Xia, W. Ho, H. Xu, M. Xie, *2D Mater.* **2022**, 9, 045002.
[39] Y. Zheng, T. J. Slade, L. Hu, X. Y. Tan, Y. Luo, Z.-Z. Luo, J. Xu, Q. Yan, M. G. Kanatzidis, *Chem. Soc. Rev.* **2021**, 50, 9022.
[40] W. Liao, S. Yau, *J. Phys. Chem. C* **2017**, 121, 19218.
[41] H. F. Waibel, M. Kleinert, L. A. Kibler, D. M. Kolb, *Electrochim. Acta* **2002**, 47, 1461.
[42] B. Qie, Z. Wang, J. Jiang, Z. Zhang, P. H. Jacobse, J. Lu, X. Li, F. Liu, A. N. Alexandrova, S. G. Louie, M. F. Crommie, F. R. Fischer, *Science* **2024**, 384, 895.
[43] R. Yin, X. Zhu, Q. Fu, T. Hu, L. Wan, Y. Wu, Y. Liang, Z. Wang, Z.-L. Qiu, Y.-Z. Tan, C. Ma, S. Tan, W. Hu, B. Li, Z. F. Wang, J. Yang, B. Wang, *Nat. Commun.* **2024**, 15, 2969.
[44] Z. Li, J. Zhuang, L. Wang, H. Feng, Q. Gao, X. Xu, W. Hao, X. Wang, C. Zhang, K. Wu, S. X. Dou, L. Chen, Z. Hu, Y. Du, *Sci. Adv.* **2018**, 4, eaau4511.
[45] Y. Li, S. Zhai, Y. Liu, J. Zhang, Z. Meng, J. Zhuang, H. Feng, X. Xu, W. Hao, M. Zhou, G.-H. Lu, S. X. Dou, Y. Du, *Adv. Sci.* **2023**, 2303483.
[46] J. Tersoff, D. R. Hamann, *Phys. Rev. B* **1985**, 31, 805.
[47] J. Xiao, B. Yan, *Nat. Rev. Phys.* **2021**, 3, 283.

[48] A. Soumyanarayanan, N. Reyren, A. Fert, C. Panagopoulos, *Nature* **2016**, 539, 509.
[49] W. Gao, X. Zhu, F. Zheng, M. Wu, J. Zhang, C. Xi, P. Zhang, Y. Zhang, N. Hao, W. Ning, M. Tian, *Nat. Commun.* **2018**, 9, 3249.
[50] N. B. M. Schröter, D. Pei, M. G. Vergniory, Y. Sun, K. Manna, F. de Juan, J. A. Krieger, V. Süss, M. Schmidt, P. Dudin, B. Bradlyn, T. K. Kim, T. Schmitt, C. Cacho, C. Felser, V. N. Strocov, Y. Chen, *Nat. Phys.* **2019**, 15, 759.
[51] Y. Liu, Y. Y. Li, S. Rajput, D. Gilks, L. Lari, P. L. Galindo, M. Weinert, V. K. Lazarov, L. Li, *Nat. Phys.* **2014**, 10, 294.
[52] Y. Hu, X. Wu, Y. Yang, S. Gao, N. C. Plumb, A. P. Schnyder, W. Xie, J. Ma, M. Shi, *Sci. Adv.* **2022**, 8, eadd2024.
[53] Y. Zhang, K. He, C.-Z. Chang, C.-L. Song, L.-L. Wang, X. Chen, J.-F. Jia, Z. Fang, X. Dai, W.-Y. Shan, S.-Q. Shen, Q. Niu, X.-L. Qi, S.-C. Zhang, X.-C. Ma, Q.-K. Xue, *Nat. Phys.* **2010**, 6, 584.
[54] P. Leng, F. Chen, X. Cao, Y. Wang, C. Huang, X. Sun, Y. Yang, J. Zhou, X. Xie, Z. Li, E. Zhang, L. Ai, Y. Yang, F. Xiu, *Nano Lett.* **2020**, 20, 7004.
[55] Q. Wu, S. Zhang, H.-F. Song, M. Troyer, A. A. Soluyanov, *Comput. Phys. Commun.* **2018**, 224, 405.
[56] A. A. Soluyanov, D. Vanderbilt, *Phys. Rev. B* **2011**, 83, 235401.
[57] G. Kresse, J. Furthmüller, *Phys. Rev. B* **1996**, 54, 11169.
[58] P. E. Blöchl, *Phys. Rev. B* **1994**, 50, 17953.
[59] J. P. Perdew, K. Burke, M. Ernzerhof, *Phys. Rev. Lett.* **1996**, 77, 3865.
[60] A. A. Mostofi, J. R. Yates, Y.-S. Lee, I. Souza, D. Vanderbilt, N. Marzari, *Comput. Phys. Commun.* **2008**, 178, 685.

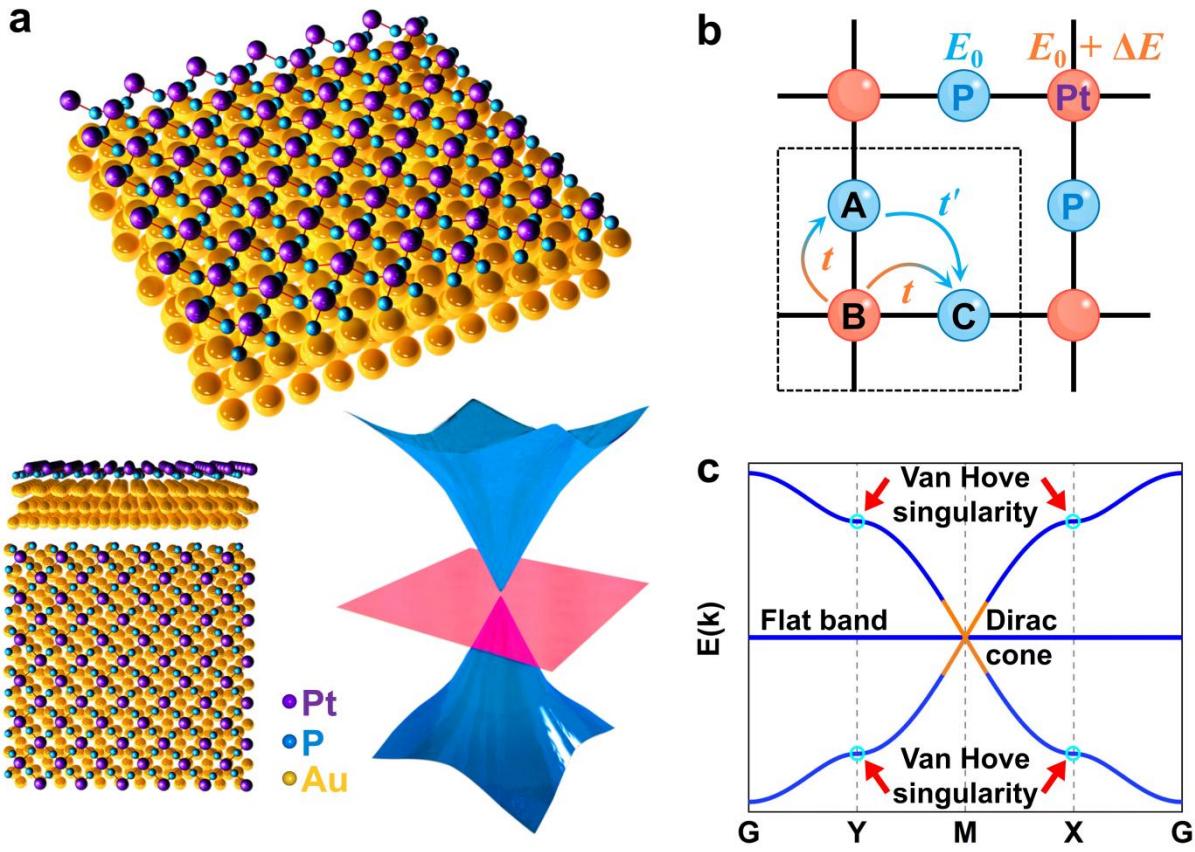

Figure 1. Basic design and tight-binding model of the Lieb lattice. (a) Schematic diagram of a Lieb lattice design, where purple/blue/golden spheres represent Pt/P/Au atoms, respectively. (b) Crystal structure of the Lieb lattice with one corner site (B) and two edge-centered sites (A and C), where orange/blue spheres represent Pt/P atoms, respectively. On-site energies are $E_0 + \Delta E$ and E_0 for B and A/C, respectively. t and t' represent the nearest-neighbor and next-nearest-neighbor hopping, respectively. The black dashed box indicates the unit cell. (c) Band structure of the Lieb lattice with nearest-neighbor electron hopping. The partial FB, Dirac cone, and VHSs are clearly seen.

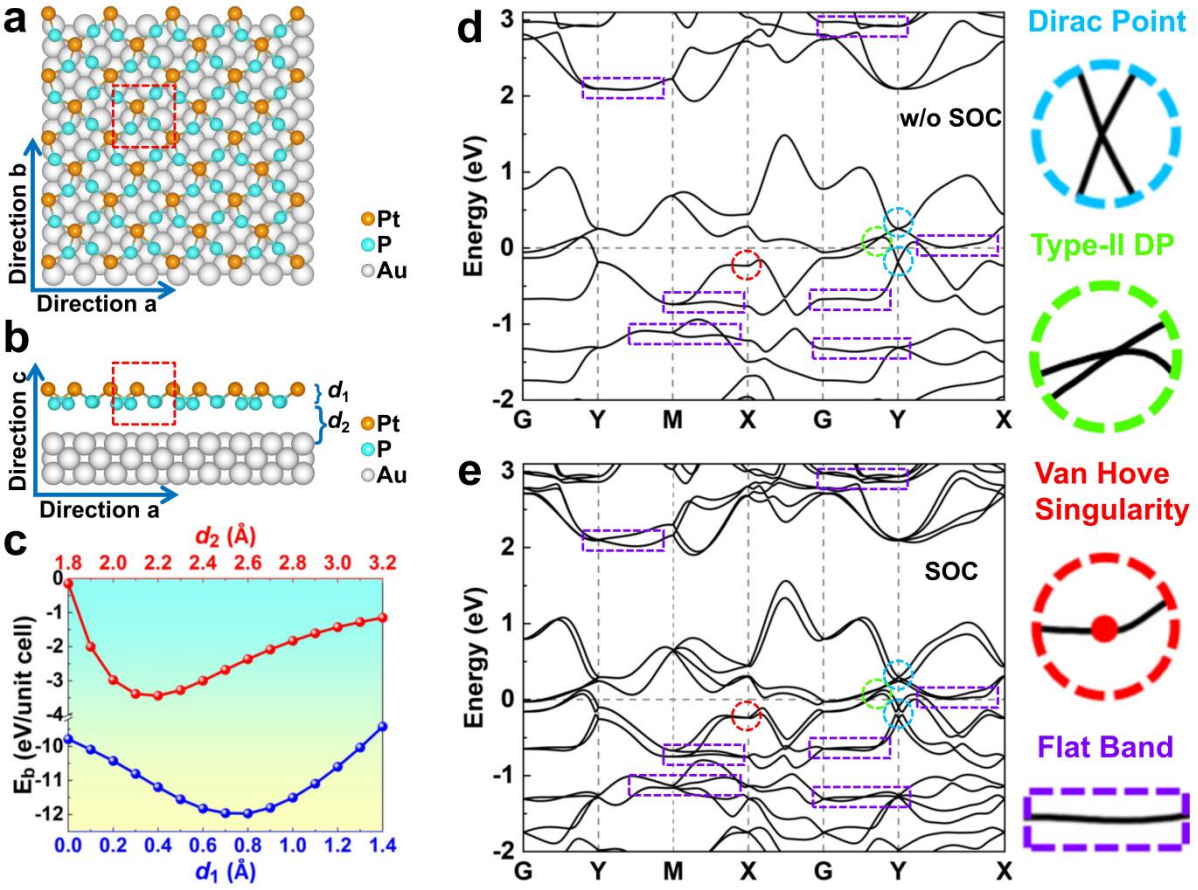

Figure 2. Crystal and electronic band structure. (a and b) Top view (a) and side view (b) of the 2D Lieb lattice composed of a $\sqrt{2} \times \sqrt{2}$ Pt and a 1×1 P square-like lattice on an Au(111) surface. The red dashed box indicates the unit cell. Orange/cyan/gray spheres represent Pt/P/Au atoms, respectively. (c) Interlayer binding energy of the 2D Lieb lattice as a function of the interlayer distances indicated in panel (b). (d and e) Calculated electronic band structure of the 2D Lieb lattice without (d) and with (e) spin-orbit coupling. Dirac points, type-II Dirac points, VHSs, and partial FBs are marked by blue, green, red, and purple dashed lines, respectively.

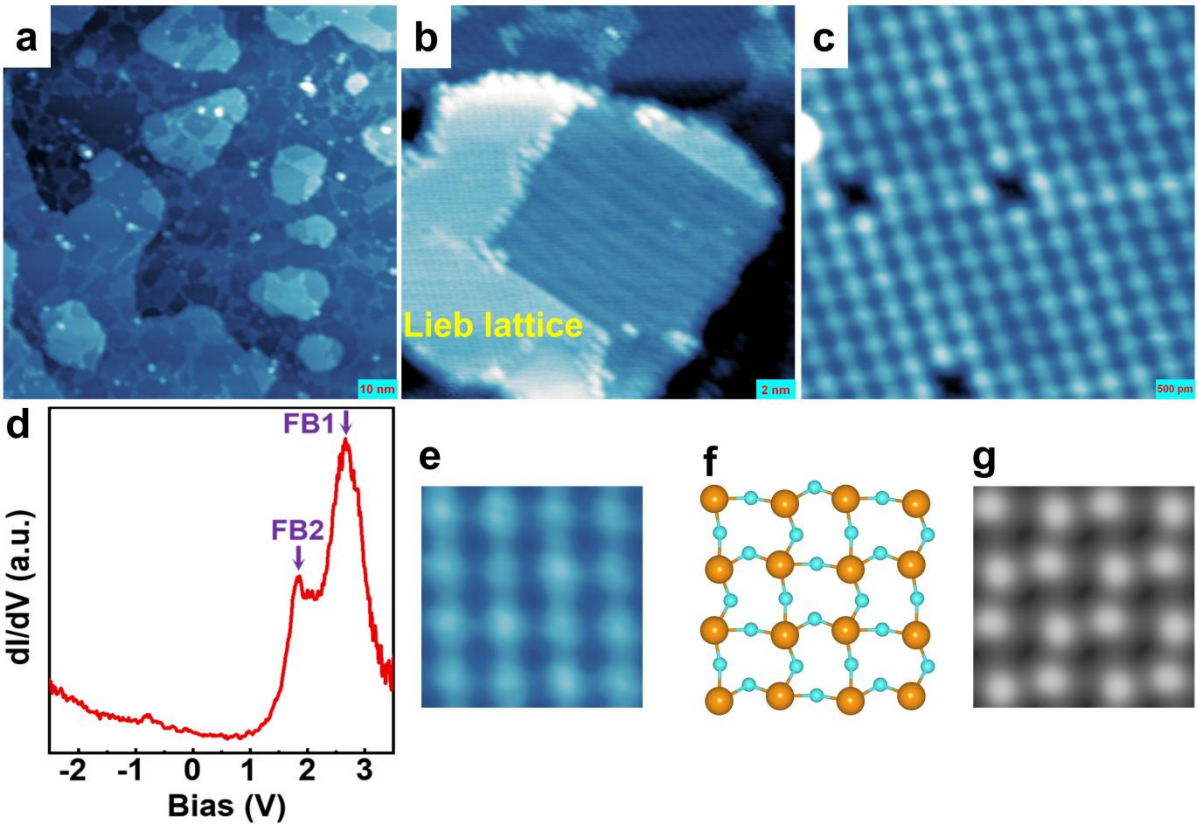

Figure 3. Lieb lattices imaged by STM and electronic FB peaks measured by STS. (a) Sample after deposition of Pt atoms and annealing at 300 ℃ for 80 min. (b) A close-up STM image, Lieb lattices exist in the bright region. (c) Atomically resolved STM image of Lieb lattices. (a) V_s = -1 V, 100 × 100 nm^2; (b) V_s = -10 mV, 20 × 20 nm^2; (c) V_s = -300 mV, 5 × 5 nm^2. (d) The dI/dV spectrum for the sites within the Lieb lattice as a function of bias voltage V, showing two FB peaks at ~ +2.66 V (FB1) and ~ +1.83 V (FB2), respectively. (e to g) Zoomed-in STM image (e), corresponding atomic model (f), and simulated STM image (g) of Lieb lattices.

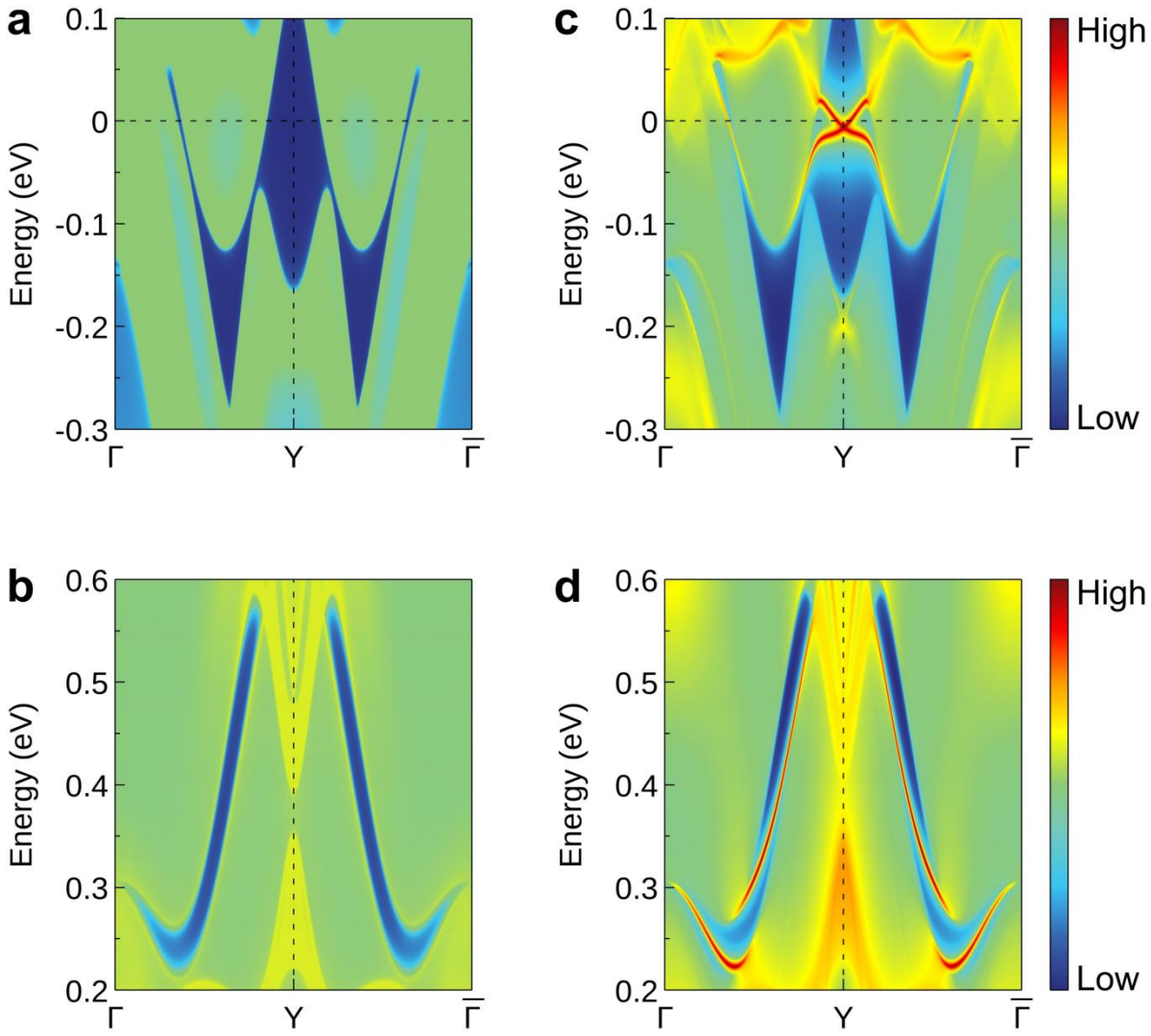

Figure 4. Prediction of topological edge states in the Pt-P Lieb lattice. (a and b) Calculated spectral function of the (100) surface states along $\Gamma - Y - \bar{\Gamma}$ paths below (a) and above (b) E_F. (c and d) Calculated spectral function of the (100) surface states and edge states along $\Gamma - Y - \bar{\Gamma}$ paths below (c) and above (d) E_F. The red contours denote the edge states.

Realization of a Two-Dimensional Lieb Lattice in a Metal-Inorganic Framework with Partial Flat Bands and Topological Edge States

Wenjun Wu,[#] Shuo Sun,[#] Chi Sin Tang,[#] Jing Wu, Yu Ma, Lingfeng Zhang,* Chuanbing Cai, Jianxin Zhong, Milorad V. Milošević, Andrew T. S. Wee, Xinmao Yin**

ToC figure

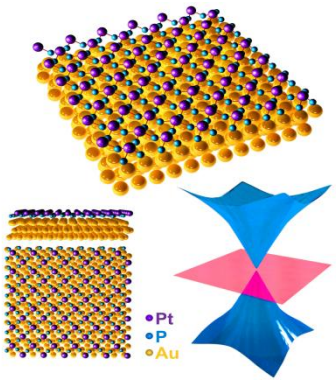

Flat bands, Dirac cones, and van Hove singularities in the Lieb lattice, unveiling a multitude of fascinating physical phenomena, are still highly sought. Here, we combine theoretical analysis with experimental validation to explore an innovative approach circumventing structural instability to realize a two-dimensional Lieb lattice, showcasing its partial flat bands and topological edge states.

Supporting Information

Realization of a Two-Dimensional Lieb Lattice in a Metal-Inorganic Framework with Partial Flat Bands and Topological Edge States

Wenjun Wu,[#] Shuo Sun,[#] Chi Sin Tang,[#] Jing Wu, Yu Ma, Lingfeng Zhang,* Chuanbing Cai, Jianxin Zhong, Milorad V. Milošević, Andrew T. S. Wee, Xinmao Yin**

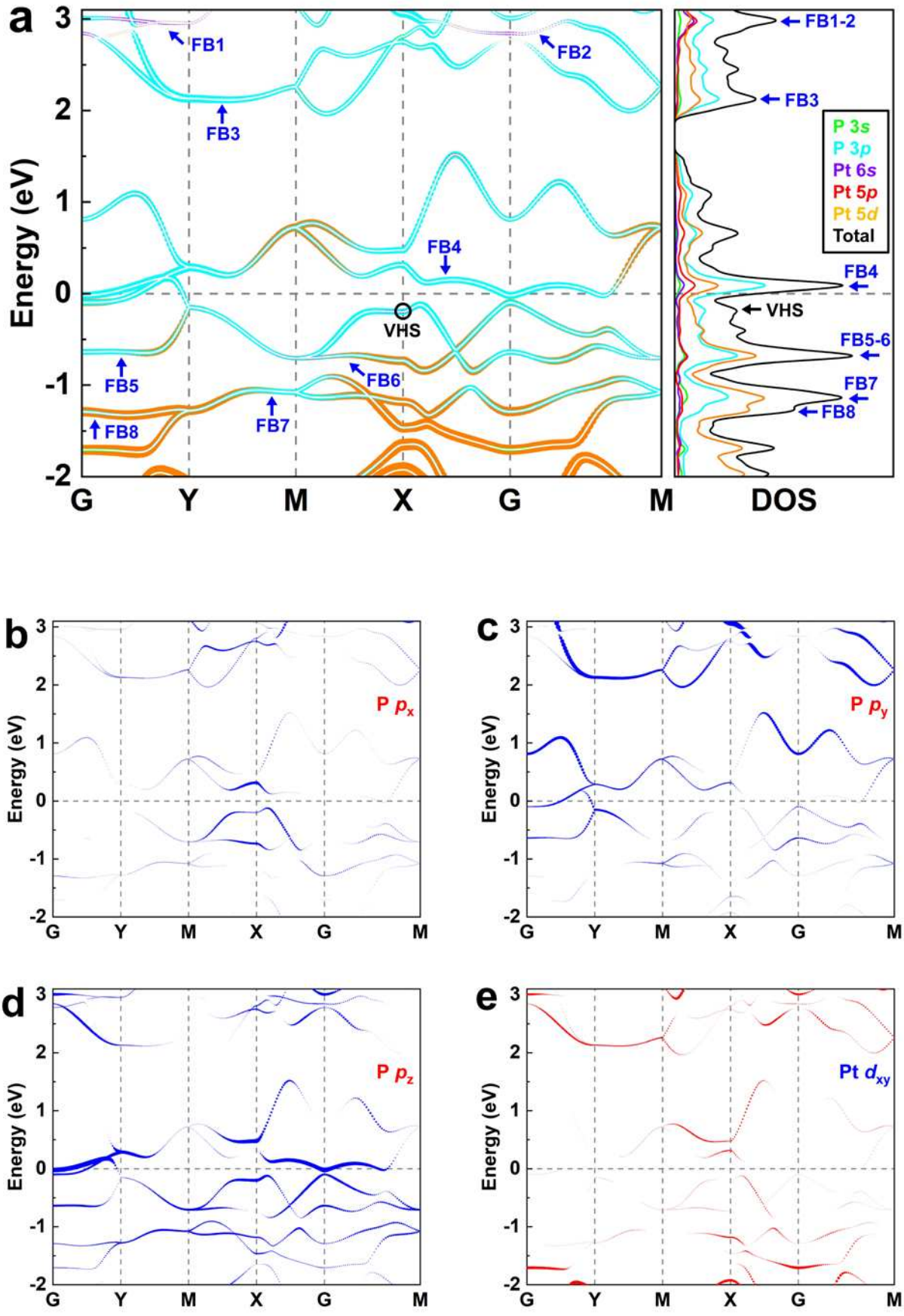
a
Energy (eV)
FB1
FB2
FB3
FB4
VHS
FB5
FB6
FB7
FB8
G
Y
M
X
G
M
DOS
FB1-2
FB3
P 3s
P 3p
Pt 6s
Pt 5p
Pt 5d
Total
FB4
VHS
FB5-6
FB7
FB8
b
P p_x
c
P p_y
d
P p_z
e
Pt d_{xy}

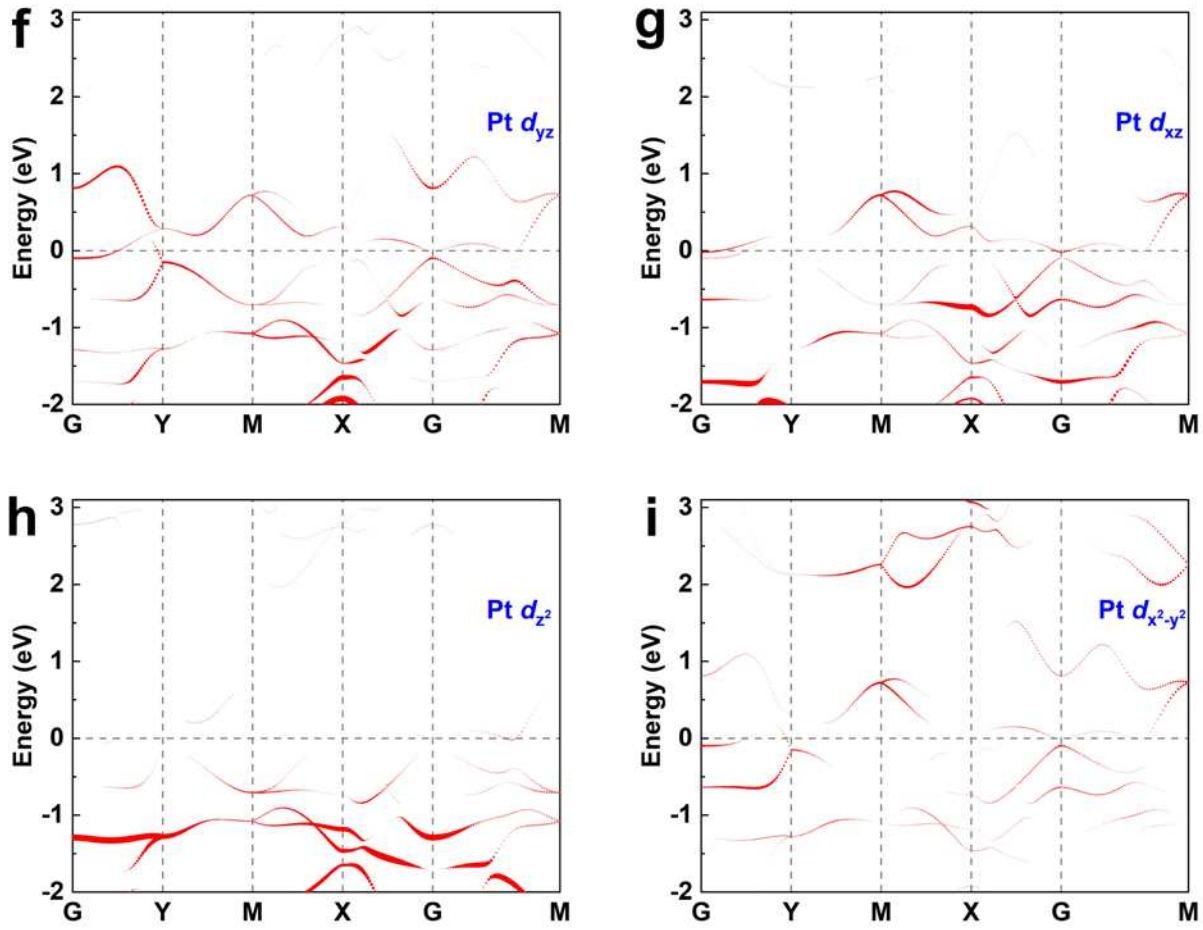

Figure S1. Electronic band structure of the Pt-P Lieb lattice. (a) Projected band structure and projected density of state (PDOS) in the Pt-P Lieb lattice. Eight partial flat bands (partial FB1-8) and corresponding PDOS peaks are marked by blue arrows. The van Hove singularity is marked by a black circle and the corresponding PDOS peak is marked by a black arrow. Orbital-decomposed band structures of P atomic p_x (b), p_y (c), p_z (d) in the Lieb lattice. Orbital-decomposed band structures of Pt atomic d_{xy} (e), d_{yz} (f), d_{xz} (g), d_{z^2} (h), $d_{x^2-y^2}$ (i) in the Lieb lattice.

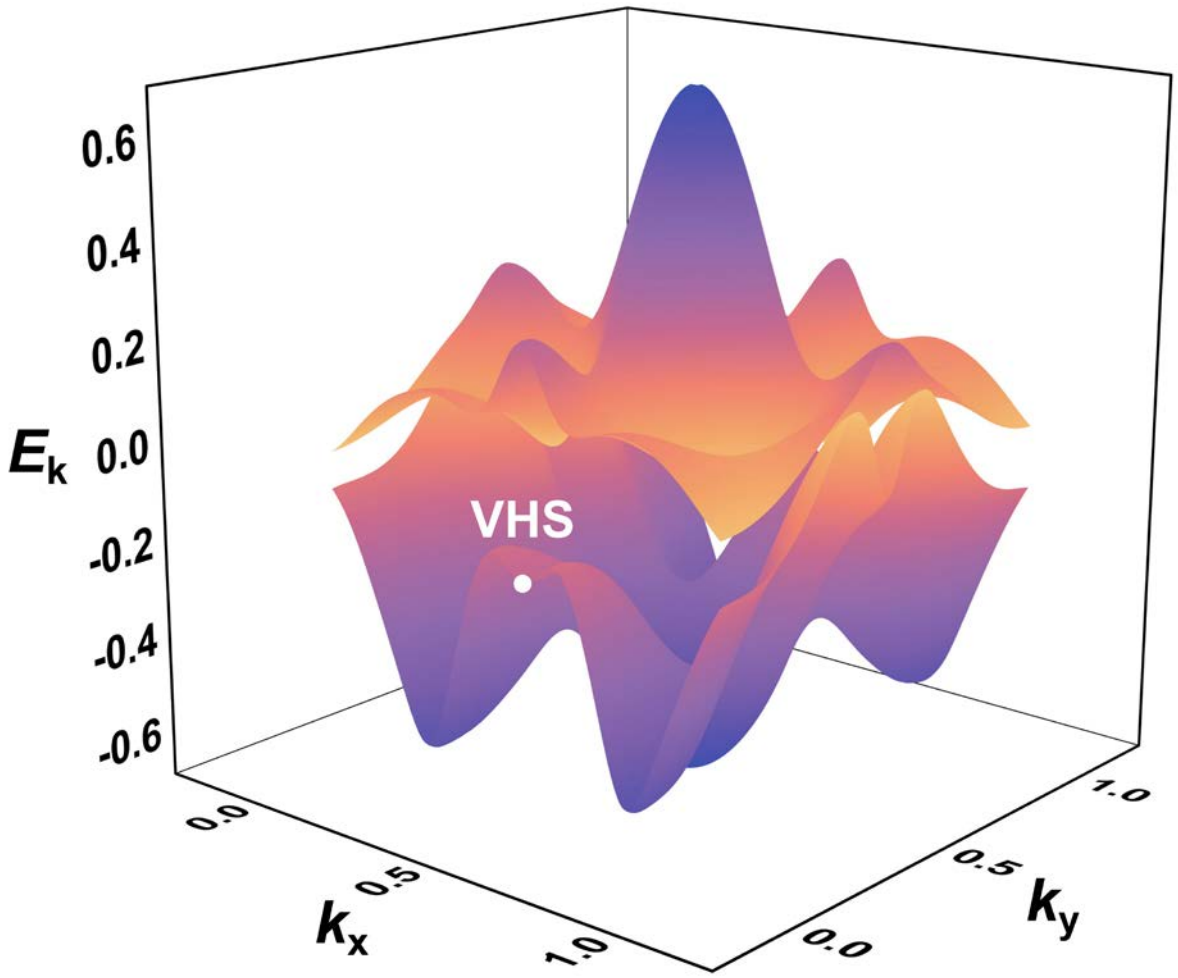

Figure S2. Schematic of a van Hove singularity (VHS) in the Pt-P Lieb lattice. Three-dimensional band structure near the Fermi level. The VHS is marked with a white dot.

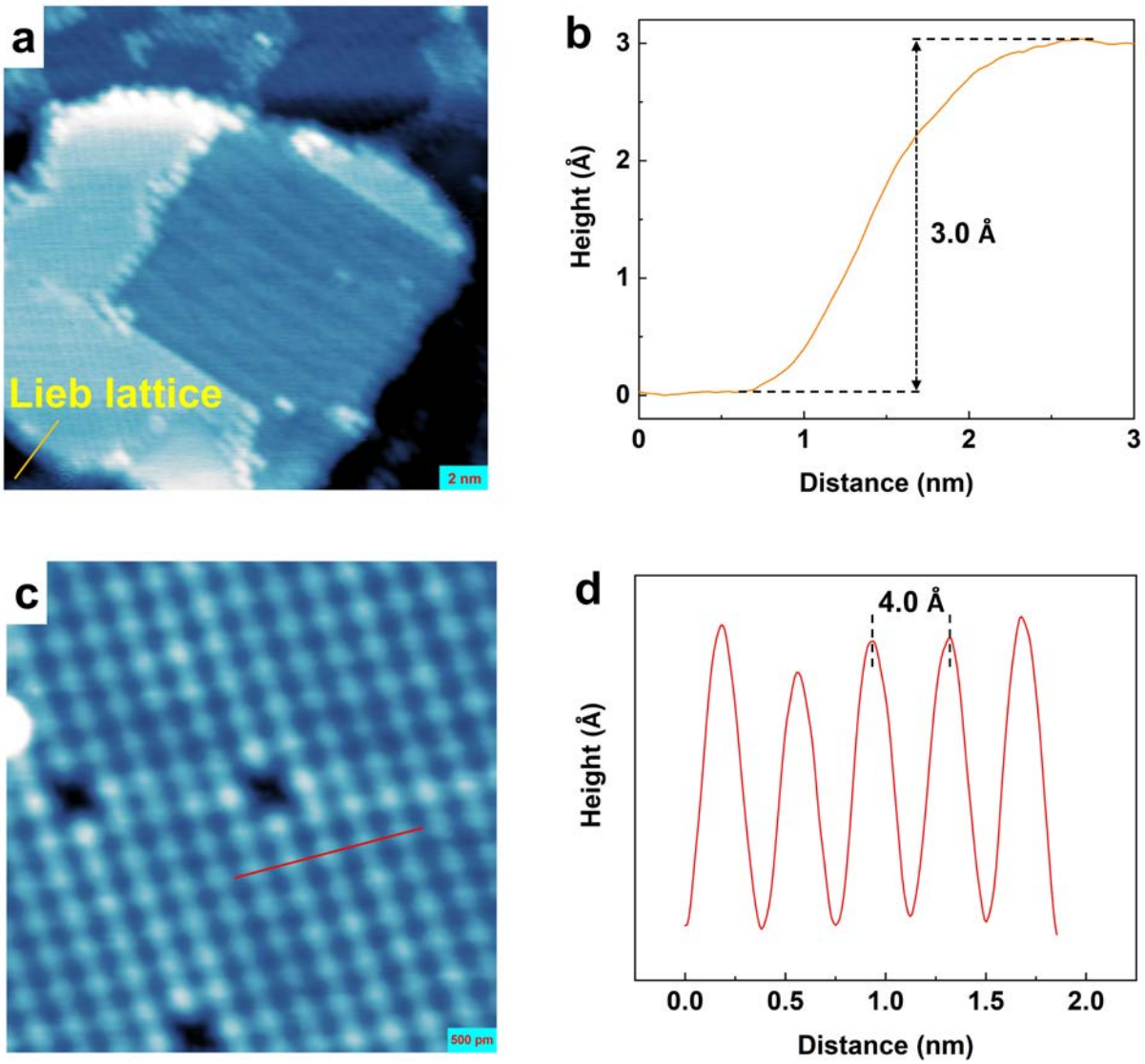

Figure S3. Pt-P Lieb lattices deposited on Au(111). (a) The close-up STM image of the Pt-P Lieb lattice on a Au(111) surface. (b) Height profile along the orange line in (a). (c) Atomically resolved STM image of Lieb lattices. (d) Line profile along the red line in (c).

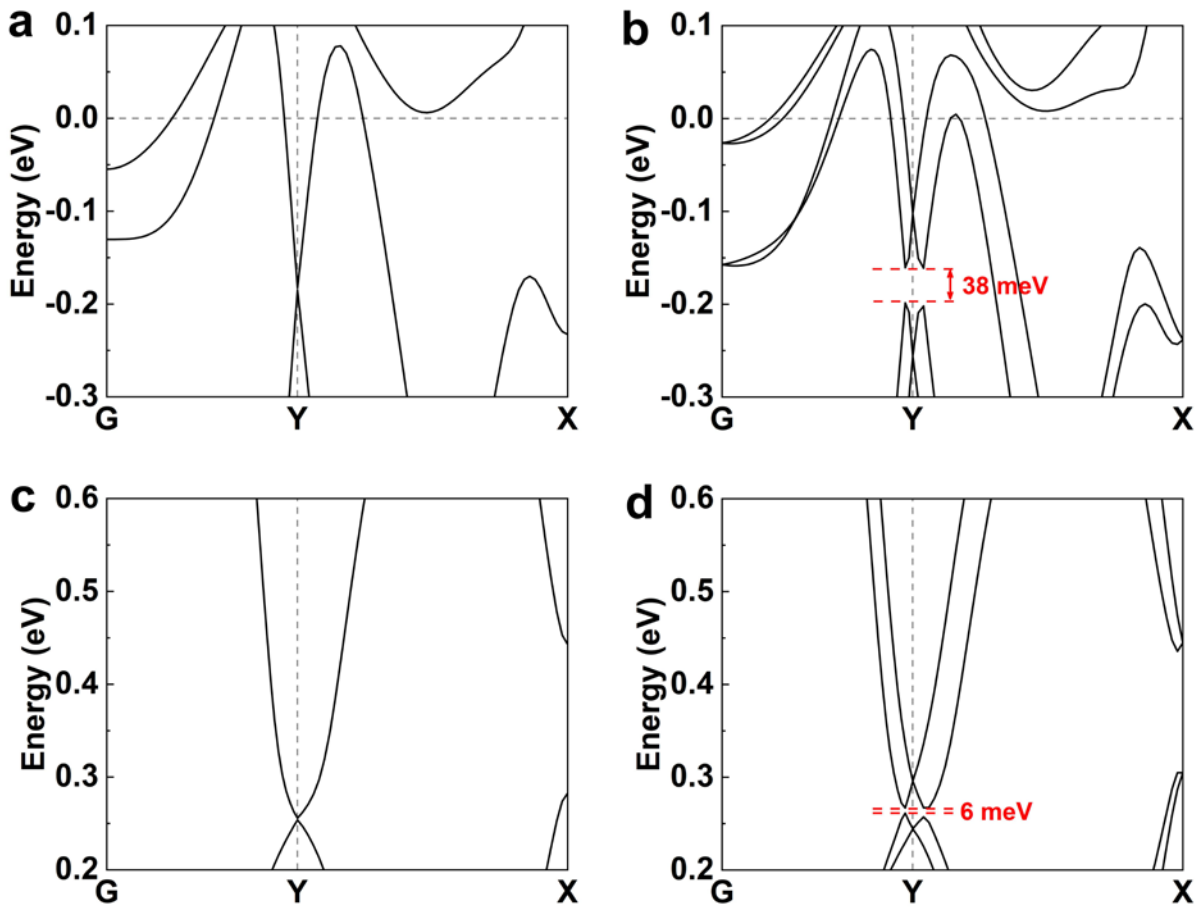

Figure S4. Magnified band structure of the Pt-P Lieb lattice. (a and b) Calculated band structure of the Pt-P Lieb lattice without (a) and with (b) spin-orbital coupling, where a bandgap opens at the Dirac cone located at ~E_F -0.18 eV by ~38 meV with spin-orbital coupling. (c and d) Calculated band structure of the Pt-P Lieb lattice without (c) and with (d) spin-orbital coupling, where a bandgap opens at the Dirac cone located at ~E_F +0.26 eV by ~6 meV with spin-orbital coupling.

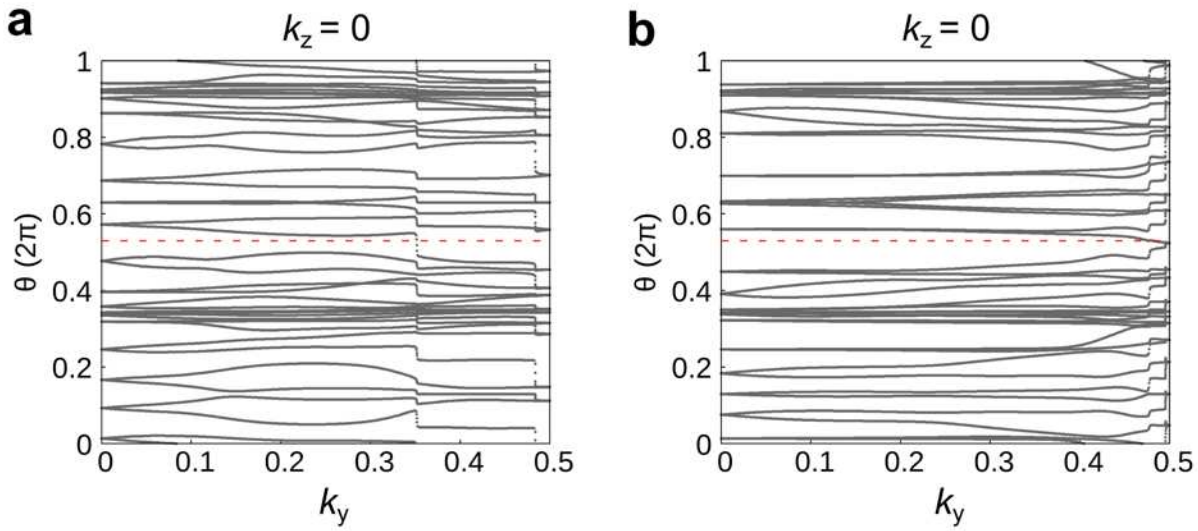

Figure S5. Z_2 topological invariants for the Pt-P Lieb lattice. (a and b) Evolution of Wannier charge centers (WCCs) for (a) $k_z = 0$ (corresponding to Fig. 4c), (b) $k_z = 0$ (corresponding to Fig. 4d) time-reversal invariant momentum planes. For the two-dimensional Lieb system, it can only take the Z_2 number at $k_z = 0$ plane. WCC evolution lines cross an arbitrary reference line (red dashed line) with an odd number of times on the $k_z = 0$ plane, resulting in $Z_2 = 1$.

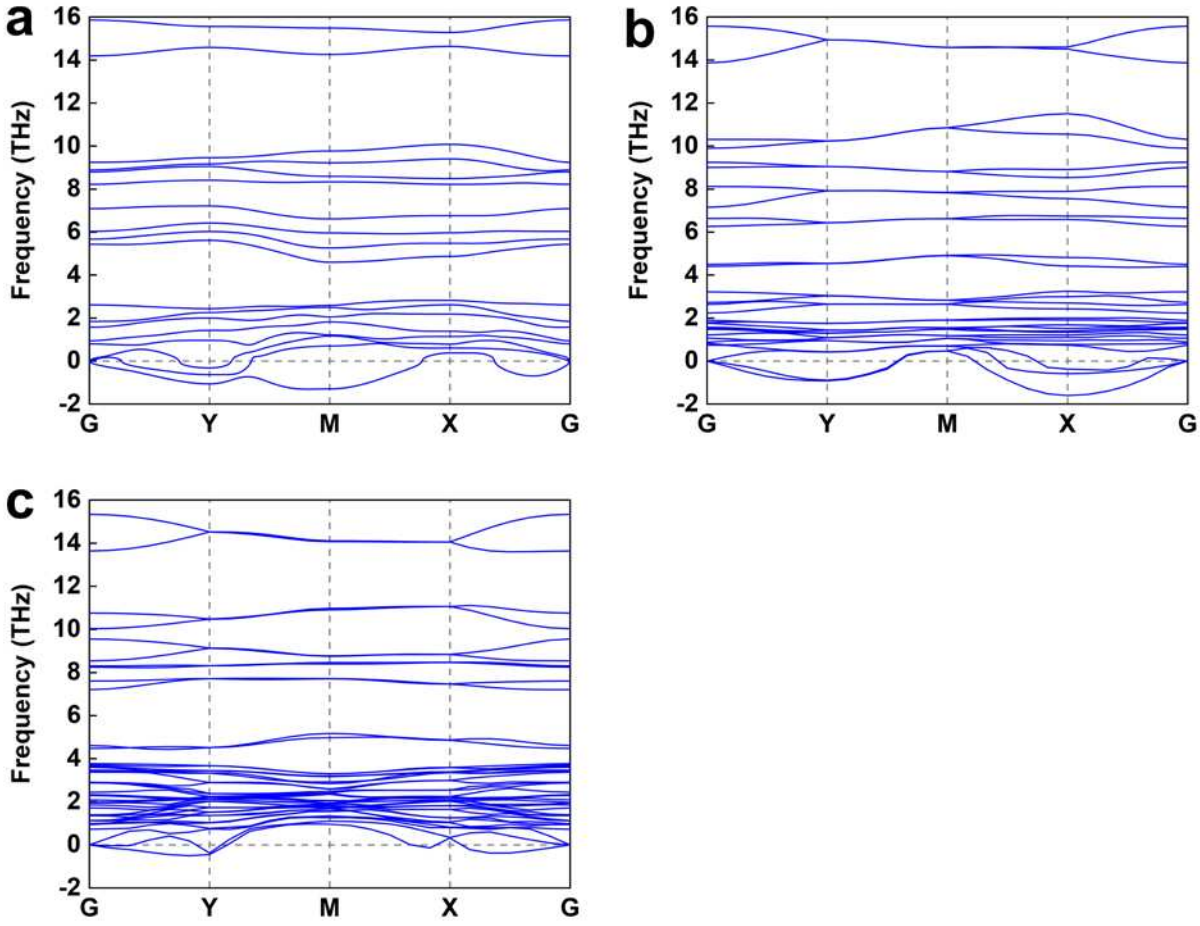

Figure S6. Phonon spectra of the Pt-P Lieb lattice. Phonon dispersion curves of the Pt-P Lieb lattice (a) and of that with a single-layer Au substrate (b), two-layer Au substrate (c).

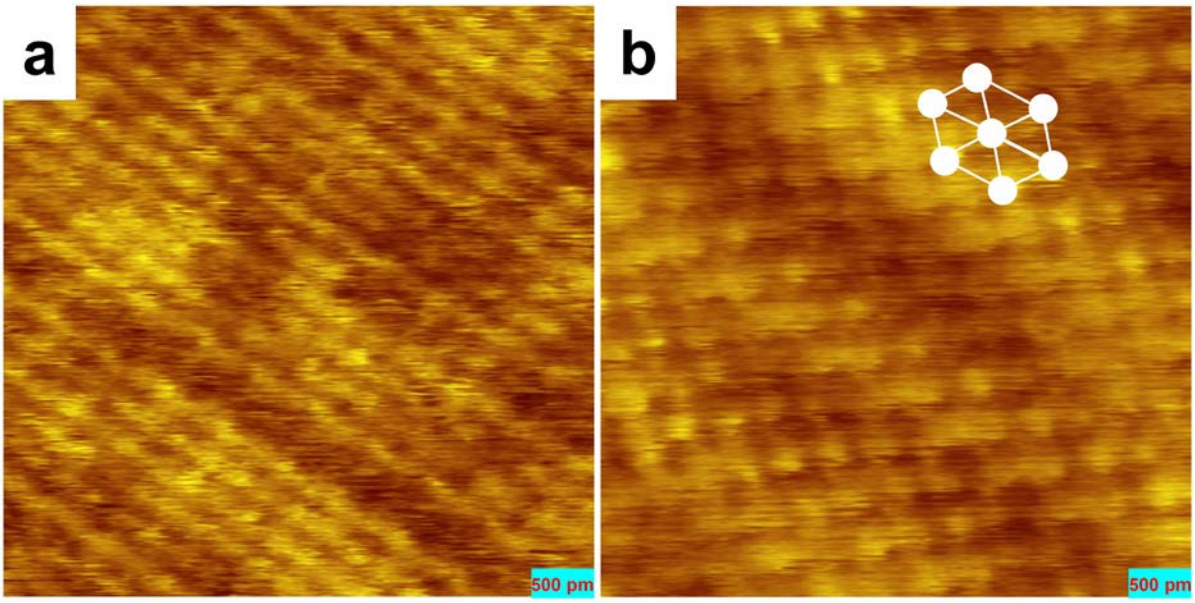

Figure S7. Dark region imaged by scanning tunneling microscopy. (a and b) Two close-up scanning tunneling microscopy images of dark region next to the Lieb lattice. (a) V_s = -10 mV, 5 × 5 nm^2; (b) V_s = -10 mV, 5 × 5 nm^2. Wherein, Pt atoms, represented by white spheres, exhibit a hexagonal shape.

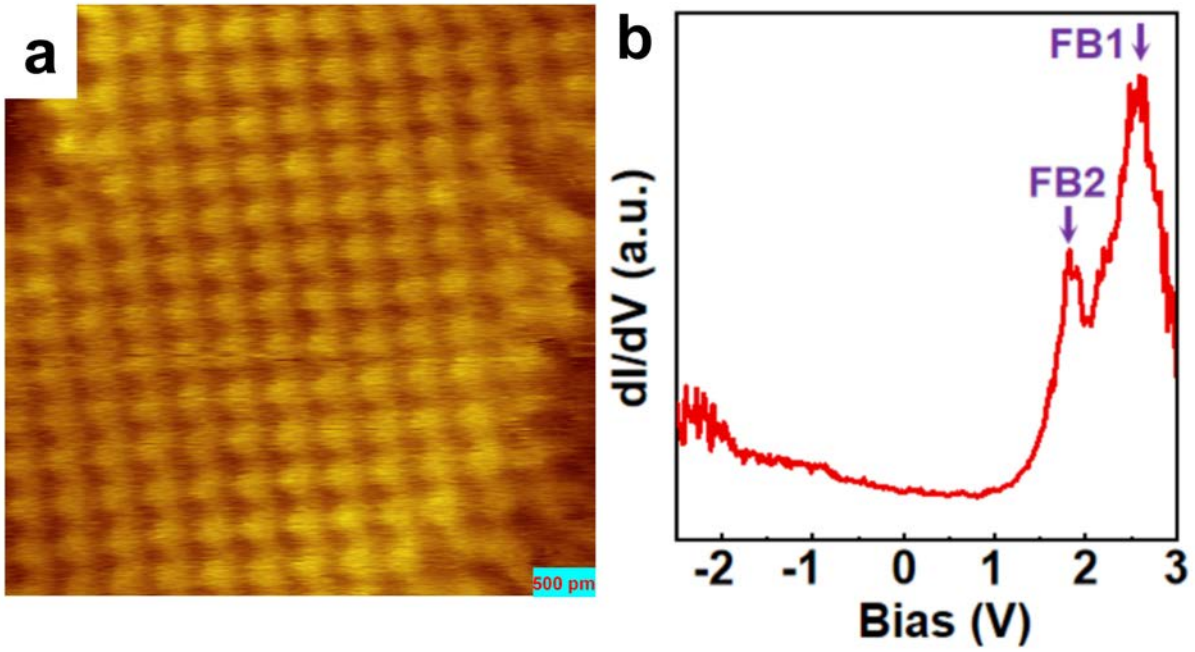

Figure S8. Lieb lattices imaged by scanning tunneling microscopy. (a) The close-up scanning tunneling microscopy image of the Pt-P Lieb lattice. V_s = -10 mV, 5 × 5 nm^2. (b) The dI/dV spectrum for the sites (a) as a function of bias voltage V.

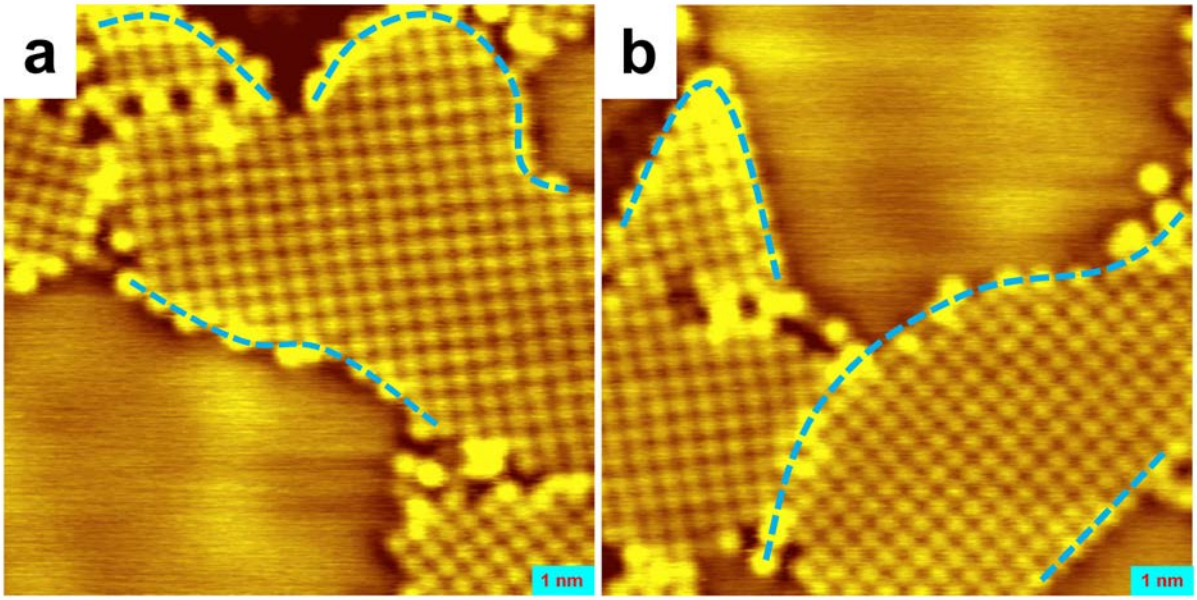

Figure S9. Lieb lattices imaged by scanning tunneling microscopy. (a and b) Two close-up scanning tunneling microscopy images of the Pt-P Lieb lattice. (a) V_s = -200 mV, 10 × 10 nm^2; (b) V_s = -200 mV, 10 × 10 nm^2. The bright features at the edge of the Lieb lattice are marked by blue dashed lines.